Supporting Information (SI)

Optimization of Nonthermal Plasma (NTP) Catalytic CO_2 Methanation: The effect of excitation waveform, pellet size and residence time

Shaowei Chen[a,b†], Yi Chen[a,b†], Jianguo Huang[a,c], Shanshan Xu[d], Xiaolei Fan[a,d,e], Jiangqi Niu [a,f,*], Huanhao Chen[b,*]

[a] *Institute of Wenzhou, Zhejiang University, 26 Fengnan Road, Wenzhou 325006, China*

[b] *State Key Laboratory of Materials-Oriented Chemical Engineering, College of Chemical Engineering, Nanjing Tech University, Nanjing 211816, China*

[c] *Xin Xin CN (Changzhi) Technology Co., 39 Zhengda South Road, Changzhi 047199, China*

[d] *Department of Chemical Engineering, School of Engineering, The University of Manchester, Oxford Road, Manchester M13 9PL, United Kingdom*

[e] *Ningbo China Beacons of Excellence Research and Innovation Institute, University of Nottingham Ningbo China, 211 Xingguang Road, Ningbo 315048, China*

[f] *Department of Chemical Systems Engineering, Graduate School of Engineering, Nagoya University, Furo-cho, Chikusa-ku, Nagoya 464-8603, Japan*

† These authors contributed equally to this work

Corresponding authors' e-mails: niujiangqinu@gmail.com (J.N.); h.chen@njtech.edu.cn (H.C.)

Contents

Note 1 Characterization of materials

X-ray diffraction (XRD) patterns of the LDH and supported Ni catalyst were recorded using a SmartLab instrument with Cu-Kα radiation at 40 kV and 30 mA (2θ range = 10°–80° with a scan speed of 10°/min). The textural properties of the LDH and catalyst were analyzed by nitrogen (N_2) sorption measurement at liquid N_2 temperature of −196 °C using Micromeritics ASAP 2460. Before the analysis, ~0.1 g of the sample was degassed at 300 °C for 3 h. Specific surface areas and pore volumes were determined using the Brunauer–Emmett–Teller (BET) and Barret–Joyner–Halenda (BJH) methods. Transmission electron microscopy (TEM) was performed using a Talos F200S G2 microscope. A small amount of catalyst was dispersed in anhydrous ethanol and subjected to ultrasonication for 5 min, then a drop of the suspension was placed onto an ultra-thin copper mesh for TEM analysis.

Note 2 Calculation of discharge power

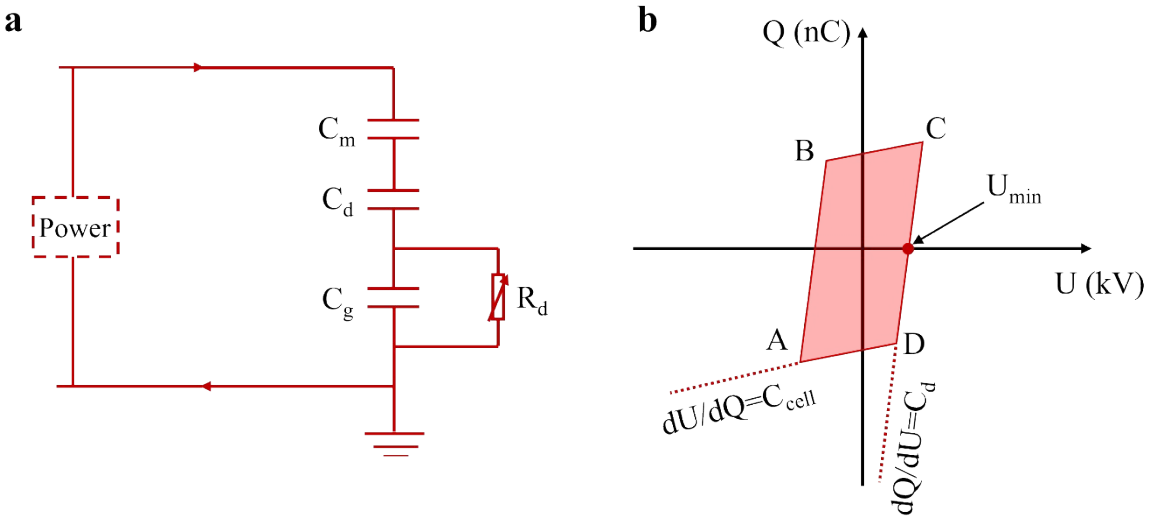

* C_m is the external capacitance for charge measurement (i.e. 2.2 μF in this work);

* C_d refers to the dielectric capacitance (i.e. the quartz tube in this study);

* C_g represents the equivalent capacitance of dielectric gap;

* C_{cell} is the total capacitance of the DBD reactor;

* R_d stands for the resistance of the plasma;

* U_{min} is the minimum external voltage at which plasma ignition occurs.

Schematic S1. (a) equivalent electrical circuit of the DBD reactor, (b) typical Lissajous figure of a DBD

In this study, the discharge power was calculation by Lissajous figure.[1] Briefly, the discharge power P is determined as the product of the voltage V and current I (Eq. S1). The voltage V was measured using a conventional high-voltage probe, while the current I was derived from the charge Q. The charge Q was

calculated as the product of the capacitor's capacitance C_m and the voltage V_m across the capacitor, measured with a differential probe (Eq. S2). Since the capacitor is connected in series within the circuit, and the current remains constant throughout, the discharge power P could be calculated using Eq. S3:

$$P(t) = V(t) \times I(t) \quad \text{Eq. S1}$$

$$I(t) = \frac{dQ(t)}{dt} = C_m \times \frac{dV_m(t)}{dt} \quad \text{Eq. S2}$$

$$P = \frac{1}{T} \times \int_0^T V(t) \times \frac{dQ(t)}{dt} \quad \text{Eq. S3}$$

where, T represents the AC cycle period.

The Q-V Lissajous curve can be obtained from the Q and V data as shown in **Figure S1**. It shows that the area inside the closed Lissajous curve divided by the AC cycle period is equal to the reactor power. Finally, we calculate P by multiplying the area inside the closed Lissajous curve and the frequency (Eq. S4).

$$P = \frac{1}{T} \times \int_0^T V(t) \times \frac{dQ(t)}{dt} = f \times S \quad \text{Eq. S4}$$

where f is the frequency and S is the area inside the closed Lissajous curve.

Additionally, C_g and U_b (breakdown voltage) were calculated according to Eq. S5 and Eq. S6 respectively, based on the DBD equivalent circuit in **Figure S1a** and the information from the Lissajous figure (**Figure S1b**).[2]

The calculation equations are as follow:

$$C_g(nF) = \frac{C_d \times C_{cell}}{C_d - C_{cell}} \quad \text{Eq. S5}$$

$$U_b(kV) = \frac{1}{1 + (C_g / C_d)} \times U_{\min} \quad \text{Eq. S6}$$

Note 3 GC analysis

GC equipped with a thermal conductivity detector (TCD) and a flame ionization detector (FID) was used to analyze the outlet gas composition online. Argon was used as the carrier gas for both detectors. In specific, the dry outlet gas (H_2, CO_2 and CO) was measured by TCD, which was separated by employing a Porapak-Q column (2 m), a GDX-502 column (2 m), and a 5A molecular sieve column (2 m). Simultaneously, the FID was used specifically for CH_4 detection by using an HP-PLOT Q column. Under steady-state conditions, for each test, at least three gas samples were collected and analyzed to calculate the averaged values with standard deviation.

Note 4 Electric field simulation method

The following explains the operational logic of Ansoft Maxwell:

Based on the finite element method (FEM) for electric field simulation, the differential equation $\phi(x,y,z)$ and its associated variational function $T(\phi)$ are established as follows:

$$T(\phi) = \frac{1}{2}\iiint_{\Omega} F(x,y,z,\phi,\phi_x,\phi_y,\phi_z)\, dx\, dy\, dz + \iint_{\Gamma} G(\phi)\, dS$$

To obtain the minimum value of the function, let $\delta F = 0$. This results in the following Euler equations:

$$\Omega: \frac{\partial F}{\partial \phi} - \frac{\partial}{\partial x}\left(\frac{\partial F}{\partial \phi_x}\right) - \frac{\partial}{\partial y}\left(\frac{\partial F}{\partial \phi_y}\right) - \frac{\partial}{\partial z}\left(\frac{\partial F}{\partial \phi_z}\right) = 0$$

$$\Gamma: \frac{\partial F}{\partial \phi_x}\cos\alpha + \frac{\partial F}{\partial \phi_y}\cos\beta + \frac{\partial F}{\partial \phi_z}\cos\gamma + \frac{\partial G}{\partial \phi} = 0$$

The functions F and G are derived from the electrostatic field potential $\phi(x,y,z)$, defined as:

$$F = \left[\left(\frac{\partial \phi}{\partial x}\right)^2 + \left(\frac{\partial \phi}{\partial y}\right)^2 + \left(\frac{\partial \phi}{\partial z}\right)^2\right] + 2\left(-\frac{\rho}{\epsilon}\phi\right)$$

$$G = -g\phi$$

By substituting F and G into the Euler equations, the following governing equation is obtained:

$$\frac{\partial^2 \phi}{\partial x^2} + \frac{\partial^2 \phi}{\partial y^2} + \frac{\partial^2 \phi}{\partial z^2} = -\frac{\rho}{\epsilon}$$

Boundary condition:

$$\Gamma_1: \phi = U_0$$

To determine the minimum threshold of the problem, the differential equation can be reformulated as:

$$minT(\phi) = \frac{1}{2}\iiint_{\Omega}\left[\left(\frac{\partial \phi}{\partial x}\right)^2 + \left(\frac{\partial \phi}{\partial y}\right)^2 + \left(\frac{\partial \phi}{\partial z}\right)^2 + 2\left(-\frac{\rho}{\epsilon}\phi\right)\right] dx\, dy\, dz + \iint_{\Gamma_1}(-g\phi)\, dS$$

Here, ϕ represents the potential in the region to be solved.

Finally, the equation is transformed from global coordinates to local coordinates, resulting in the finite element equation:

$$[K][\phi] = [0]$$

By solving this control equation using Ansoft Maxwell, the electric field distribution of the electrode can be determined. Due to the generic nature of the software and the length limitations of this article, further implementation details are not included.

Supporting figures and tables

Figure S2 shows the characteristic diffraction peaks of the hydrotalcite structure of LDH at 2θ = 11.5°, 23.9°, 35°, and 39.8°, corresponding to the (003), (006), (012), and (015) planes, respectively.[3] However, in the XRD pattern of Ni/$MgAlO_x$, no diffraction peaks related to LDH were observed. Instead, peaks corresponding to MgO (43.6° and 63.4°) and the spinel phase $MgAl_2O_4$ (37°) appeared, being consistent with findings reported elsewhere.[4] This could be attributed to the thermal treatment of the catalyst (calcined in air at 450 ℃ for 2 hours), which led to the dehydration of the LDH support.

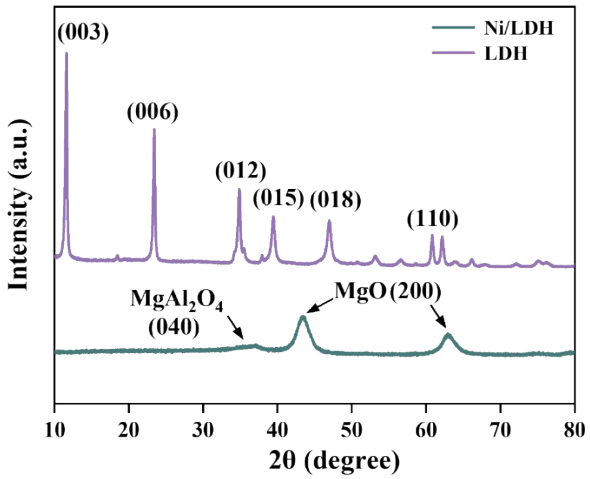

Figure S1. XRD patterns of the LDH and the reduced Ni/$MgAlO_x$ catalyst.

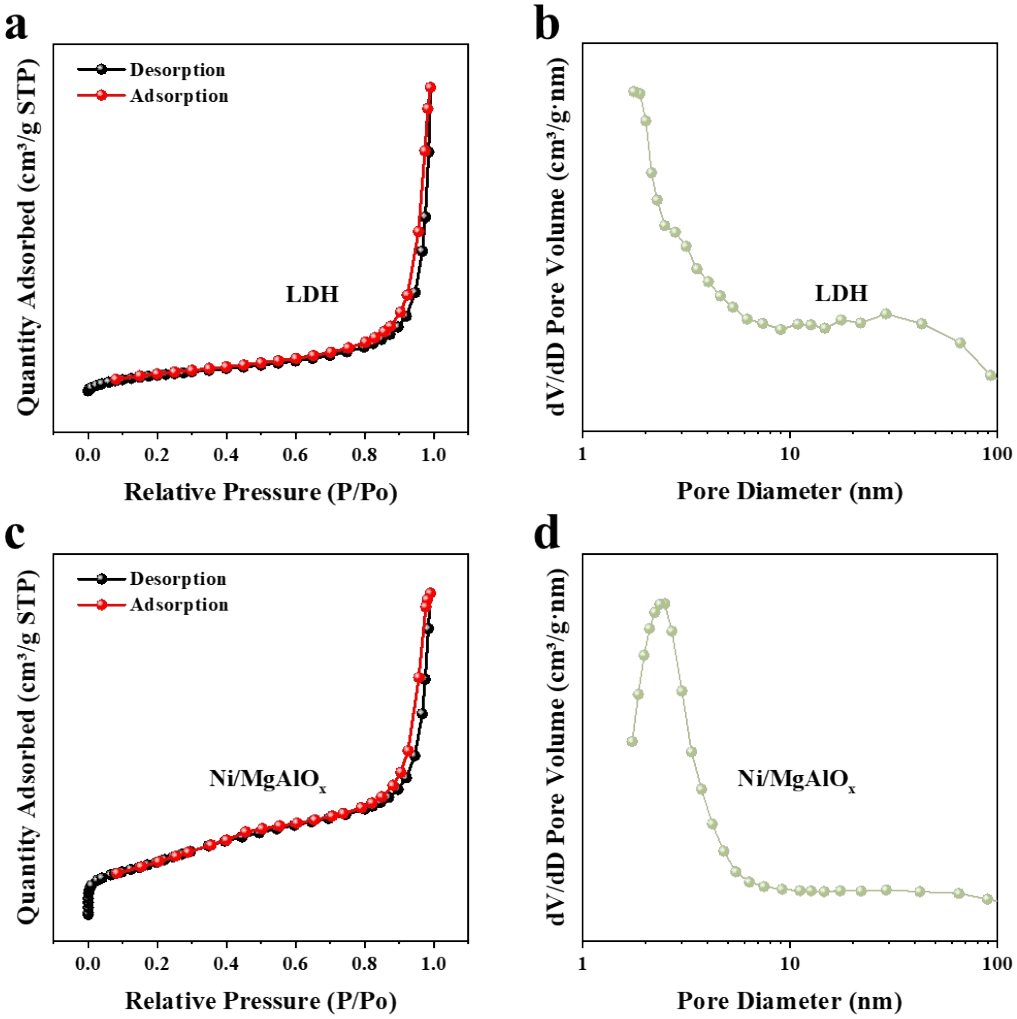

Figure S2. N_2 adsorption-desorption isotherms: (a) LDH and (c) Ni/MgAlO$_x$; pore size distribution (PSD): (b) LDH and (d) Ni/MgAlO$_x$.

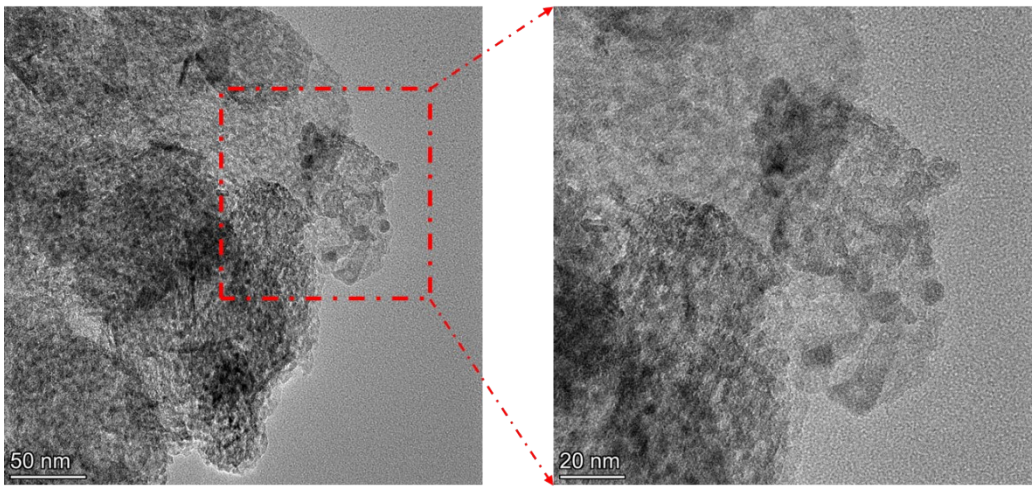

Figure S3. HRTEM images of Ni/MgAlO$_x$ at different resolutions

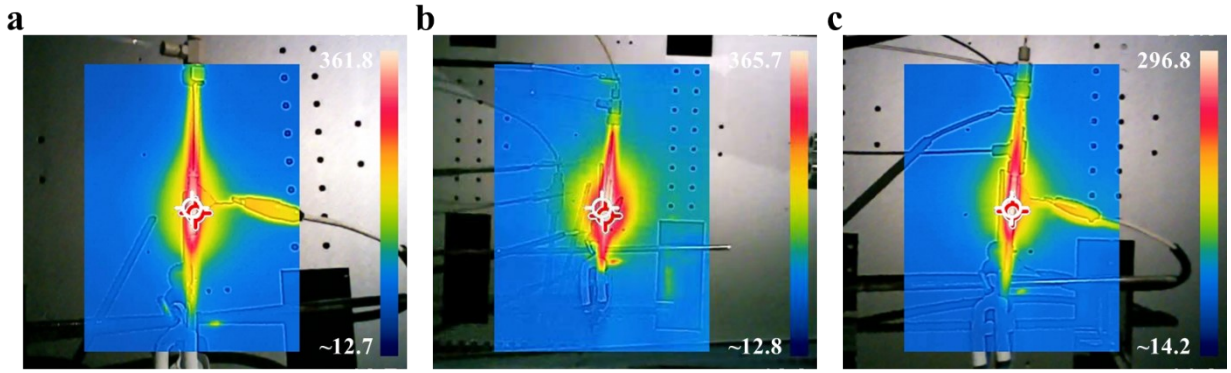

Figure S4. Temperature measurements of the NTP catalytic CO_2 methanation over the Ni/MgAlO$_x$ catalyst in three different waveform types: (a) sine wave, (b) single-pulse wave, (c) multi-pulse wave. (Experimental conditions: ~680 mg Ni/MgAlO$_x$, pellet sizes: 500–600 μm, discharge length = ~50 mm, feed gas composition = 80 vol.%H_2/20 vol.%CO_2, total flow rate = 50 mL/min, and the excitation information have been detailed in **Table S2**).

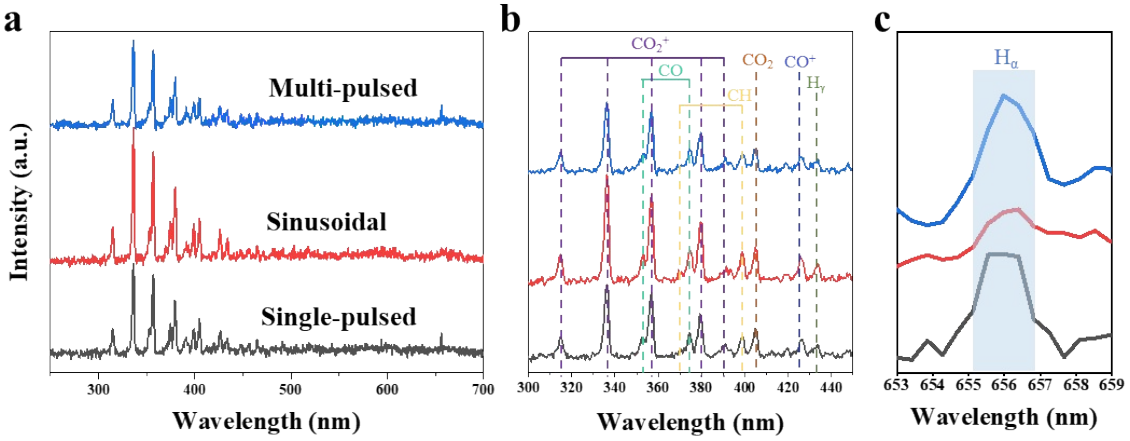

Figure S5. OES spectra at various ranges of the NTP catalytic CO_2 methanation over the Ni/MgAlO$_x$ catalyst in three different waveform types: (a) 250–700 nm, (b) 300–450 nm, (c) 653–659 nm. (Experimental conditions: ~680 mg Ni/MgAlO$_x$, pellet sizes: 500–600 μm, discharge length = ~50 mm, feed gas composition = 80 vol.%H_2/20 vol.%CO_2, total flow rate = 50 mL/min, and the excitation information have been detailed in **Table S2**).

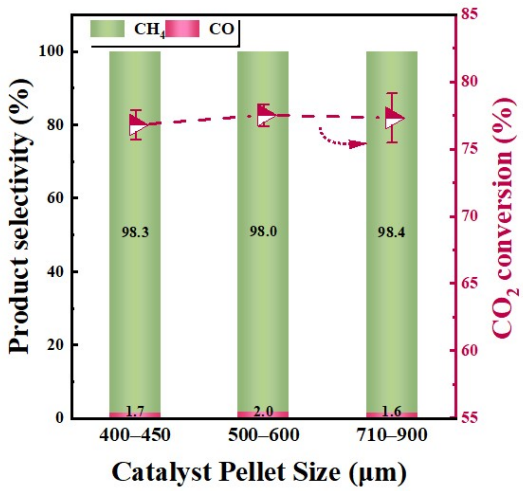

Figure S6. Performance of NTP catalytic CO_2 methanation over the Ni/MgAlO_x catalyst with different pellet sizes under multi-pulse waveform. (Experimental conditions: applied voltage = 6.0 kV, frequency = 15 kHz, pulse width = 4.7 μs, discharge power = 28 W, discharge length = ~52 mm, feed gas composition = 80 vol.%H_2/20 vol.%CO_2, total flow rate = 50 mL/min)

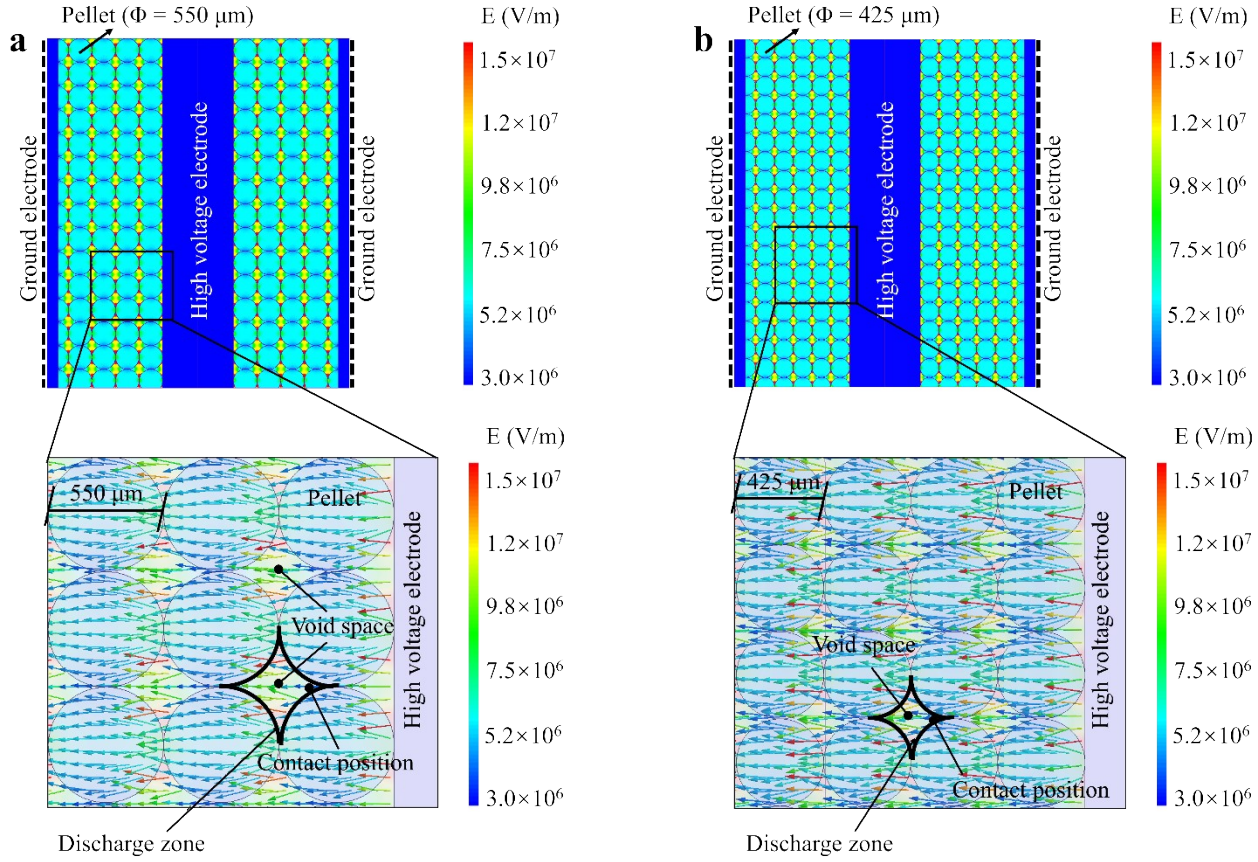

Figure S7. Schematic of the local electric field shown in packed bed with pellet of (a) 550 μm and (b) 425 μm.

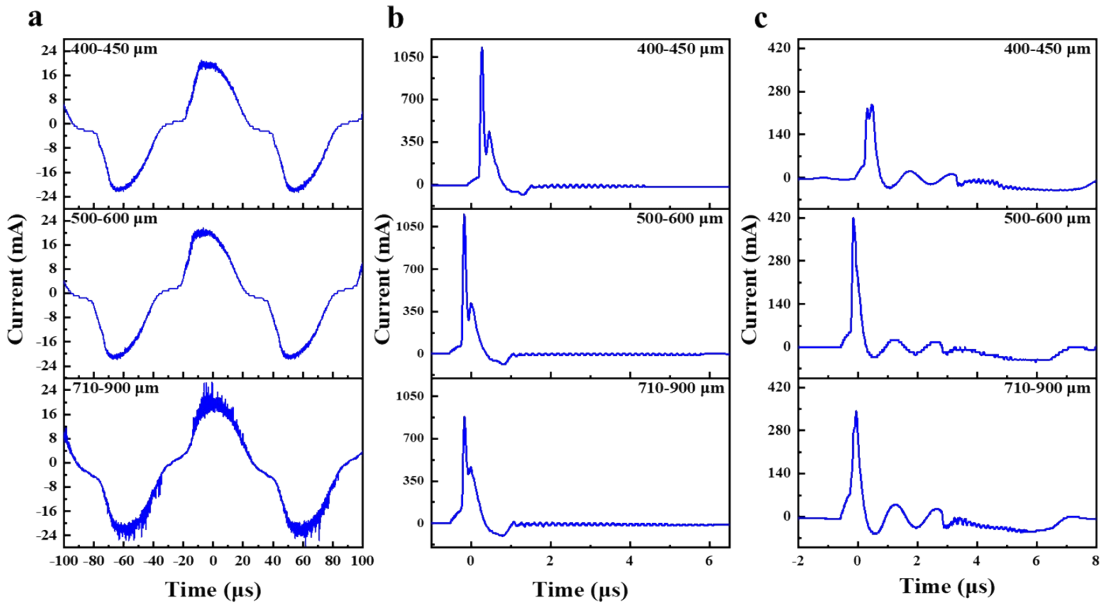

Figure S8. Instantaneous current signals of catalysts with different pellet sizes under different waveform types: (a) sine wave, (b) single-pulse wave, (c) multi-pulse wave (Experimental conditions: discharge length = ~52 mm, feed gas composition = 80 vol.%H_2/20 vol.%CO_2, total flow rate = 50 mL/min, and the excitation information have been detailed in **Table S3**)

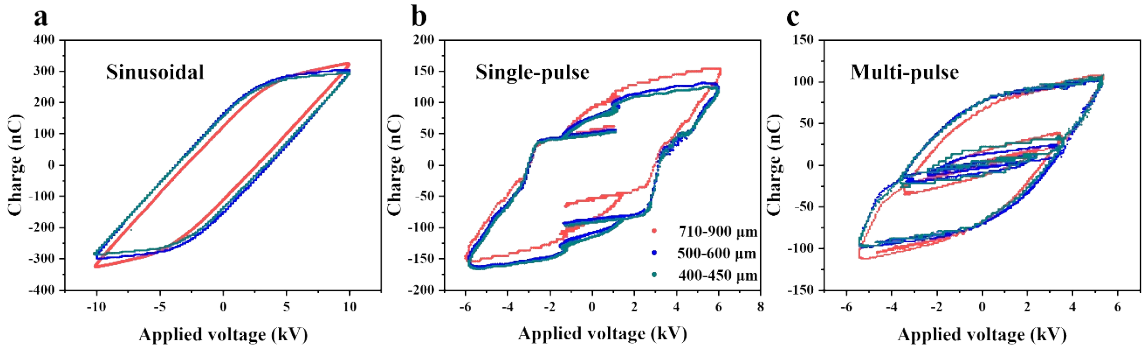

Figure S9. Lissajous figures of the NTP-catalytic CO_2 methanation over the Ni/$MgAlO_x$ catalyst with different pellet sizes under three waveform types: (a) sinusoidal, (b) single-pulse, (c) multi-pulse. (Experimental conditions: discharge length = ~52 mm, feed gas composition = 80 vol.%H_2/20 vol.%CO_2, total flow rate = 50 mL/min, and excitation information have been detailed in **Table S3**).

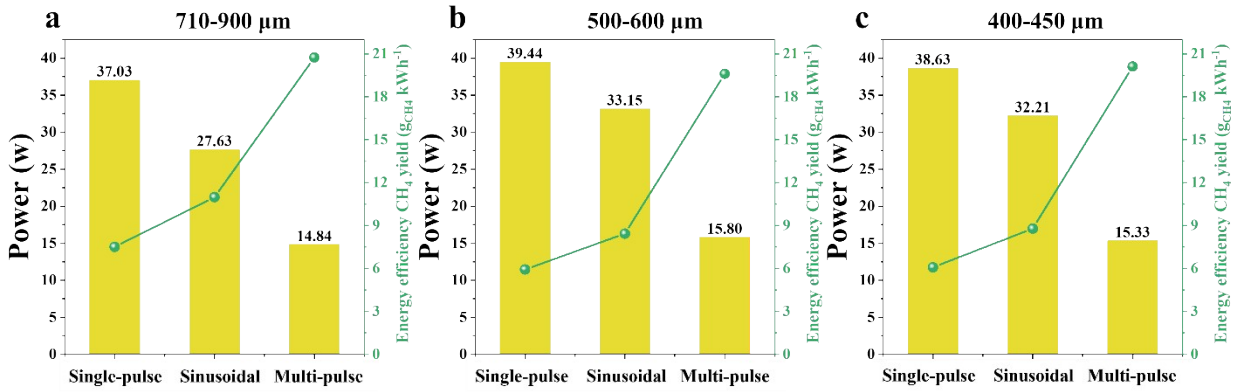

Figure S10. Energy consumption and energy efficiency based on CH_4 formation for the NTP-catalytic CO_2 methanation over the Ni/$MgAlO_x$ catalyst with different pellet sizes under three waveform types: (a) 710–900 µm, (b) 500–600 µm, (c) 400–450 µm (Experimental conditions: discharge length = ~52 mm, feed gas composition = 80 vol.%H_2/20 vol.%CO_2, total flow rate = 50 mL/min, and the excitation information have been detailed in **Table S3**).

Table S1. Textural properties of LDH and Ni/MgAlO$_x$.

Sample	Specific surface areas (m^2/g)			Specific pore volumes (cm^3/g)		
	S_{BET}	S_{micro}	S_{ext}	V_{total}	V_{micro}	V_{meso}
LDH	35	1	34	0.23	0.01	0.22
Ni/MgAlO$_x$	197	55	142	0.48	0.03	0.45

Table S2. Detailed excitation information for **Figures 3**, **4** and **Figure S5**

Excitation waveform types	Pellet size (μm)	Current (mA)	Peak voltage (kV)	Frequency (kHz)	Discharge power (W)	Pulse width (μs)
Sinusoidal	500–600	~22	10	8.5	33.2	-
Single-pulse	500–600	~1150	6	25	39.4	4.7
Multi-pulse	500–600	~400	5.3	15	15.8	10

Table S3. Detailed excitation information for **Figures 5** and **Figure S8–S10**.

Excitation waveform types	Pellet size (μm)	Current (mA)	Peak voltage (kV)	Frequency (kHz)	Discharge power (W)	Pulse width (μs)
Sinusoidal	400–450	~22	10	8.5	32.2	-
Sinusoidal	500–600	~22	10	8.5	33.2	-
Sinusoidal	710–900	~25	10	8.5	27.6	-
Single-pulse	400–450	~1150	6	25	38.6	4.7
Single-pulse	500–600	~1150	6	25	39.4	4.7
Single-pulse	710–900	~900	6	25	37.0	4.7
Multi-pulse	400–450	~250	5.3	15	15.3	10
Multi-pulse	500–600	~400	5.3	15	15.8	10
Multi-pulse	710–900	~350	5.3	15	14.8	10

Table S4. Detailed data information for **Figure 6e**.

Pellet size (μm)	Excitation voltage (kV)	Area of discharge zone (μm^2)	E of void space ($\times 10^6$ V/m)	E of contact position ($\times 10^6$ V/m)
425	9	38834	1.056	39.8
550	9	65038	1.051	47.2
805	9	139325	1.049	47.4

Table S5. Detailed excitation information for **Figure S9**.

Excitation waveform types	Pellet size (μm)	C_d (nF)	C_{cell} (nF)	C_g (nF)	U_{min} (kV)	U_b (kV)
Sinusoidal	400–450	40.1	4.9	5.6	3.4	3.0
Sinusoidal	500–600	41.4	4.7	5.4	3.4	3.0
Sinusoidal	710–900	42.4	10.7	14.3	2.7	2.0
Single-pulse	400–450	35.4	9.8	13.6	3.2	2.3
Single-pulse	500–600	34.2	9.6	13.3	3.1	2.2
Single-pulse	710–900	34.7	18.7	40.3	3.0	1.4
Multi-pulse	400–450	44.1	10.6	14.0	2.9	2.1
Multi-pulse	500–600	46.1	10.9	14.3	3.0	2.3
Multi-pulse	710–900	45.7	14.8	21.9	2.6	1.8

Table S6. Detailed data information for **Figures 7a–c**.

Excitation waveform types	Residence time (s)	Flow rate (mL/min)	CO_2 conversion (%)	CH_4 selectivity (%)	CH_4 yield (%)
Sinusoidal	1.76	25	75.1	98.1	73.7
Sinusoidal	0.88	50	73.2	96.7	70.8
Sinusoidal	0.44	100	68.4	93.3	63.9
Sinusoidal	0.29	150	64.9	90.6	58.8
Sinusoidal	0.24	180	61.0	87.2	53.2
Sinusoidal	0.20	220	58.1	84.7	49.2
Single-pulse	1.76	25	71.2	93.4	66.5
Single-pulse	0.88	50	70.7	91.8	64.9
Single-pulse	0.44	100	67.3	86.7	58.3
Single-pulse	0.29	150	65.7	84.6	55.6
Single-pulse	0.24	180	61.5	82.4	50.7
Single-pulse	0.20	220	59.3	77.7	46.1
Multi-pulse	1.76	25	74.0	98.8	73.1
Multi-pulse	0.88	50	72.9	98.5	71.8
Multi-pulse	0.44	100	71.3	95.6	68.2
Multi-pulse	0.29	150	71.1	93.3	66.3
Multi-pulse	0.24	180	70.3	90.2	63.4
Multi-pulse	0.20	220	69.1	90.8	62.8
Multi-pulse (25 mm)	0.43	50	73.2	98.2	72.3

Table S7. Detailed excitation information for **Figure 7**

Excitation waveform types	Residence time (s)	Flow rate (mL/min)	Current (mA)	Peak voltage (kV)	Frequency (kHz)	Discharge power (W)	Pulse width (μs)
Sinusoidal	1.76	25	~25	10	8.5	~28	-
Sinusoidal	0.88	50	~25	10	8.5	27.6	-
Sinusoidal	0.44	100	~25	10	8.5	~28	-
Sinusoidal	0.29	150	~24	10	8.5	~28	-
Sinusoidal	0.24	180	~23	10	8.5	~28	-
Sinusoidal	0.20	220	~23	10	8.5	~28	-
Single-pulse	1.76	25	~900	6	25	~37	4.7
Single-pulse	0.88	50	~900	6	25	37.0	4.7
Single-pulse	0.44	100	~900	6	25	~37	4.7
Single-pulse	0.29	150	~900	6	25	~37	4.7
Single-pulse	0.24	180	~900	6	25	~37	4.7
Single-pulse	0.20	220	~900	6	25	~37	4.7
Multi-pulse	1.76	25	~350	5.3	15	~15	10
Multi-pulse	0.88	50	~350	5.3	15	14.8	10
Multi-pulse	0.44	100	~350	5.3	15	~15	10
Multi-pulse	0.29	150	~350	5.3	15	~15	10
Multi-pulse	0.24	180	~350	5.3	15	~15	10
Multi-pulse	0.20	220	~350	5.3	15	~15	10
Multi-pulse (25 mm)	0.43	50	~100	5.3	15	~5	10

References

1. R. Wang, Y. Yang, S. Chen, H. Jiang and P. Martin, *IEEE TRANSACTIONS ON PLASMA SCIENCE*, 2021, **49**, 2210-2216.
2. X. Tu, H. J. Gallon, M. V. Twigg, P. A. Gorry and J. C. Whitehead, *Journal of Physics D: Applied Physics*, 2011, **44**, 274007.
3. S. Xu, S. Chansai, Y. Shao, S. Xu, Y.-c. Wang, S. Haigh, Y. Mu, Y. Jiao, C. E. Stere, H. Chen, X. Fan and C. Hardacre, *Applied Catalysis B: Environmental*, 2020, **268**, 118752.
4. Y. Zhang, S. Li, B. Qiu, S. Chen, H. Chen and X. Fan, *Chemical Engineering and Processing - Process Intensification*, 2024, **195**, 109608.